Journal of Power Sources 195 (2010) 588–592

Contents lists available at ScienceDirect

Journal of Power Sources

journal homepage: www.elsevier.com/locate/jpowsour

Short communication

Optimization of MoO_3 nanoparticles as negative-electrode material in high-energy lithium ion batteries

Leah A. Riley[a], Se-Hee Lee[a], Lynn Gedvilias[b], Anne C. Dillon[b,*]

[a] University of Colorado, Department of Mechanical Engineering, 111 Engineering Drive, Boulder, CO 80309, United States
[b] National Renewable Energy Laboratory, 1617 Cole Boulevard, Golden, CO 80401, United States

ARTICLE INFO

Article history:
Received 17 June 2009
Received in revised form 6 August 2009
Accepted 8 August 2009
Available online 15 August 2009

Keywords:
Molybdenum oxide
Anode
Nanoparticles
Annealing
Lithium-ion battery
Temperature programmed desorption

ABSTRACT

Highly uniform MoO_3 nanoparticles, created using a unique hot-wire chemical vapor deposition (HWCVD) system, were studied as active material for negative electrodes in high-energy lithium ion batteries. Transmission electron microscopy (TEM), surface area analysis (BET), and X-ray diffraction (XRD) were utilized for powder characterization. Electrodes were fabricated from a slurry of MoO_3, acetylene black (AB), and polyvinylidene fluoride (PVDF) binder deposited on copper foil. Electrochemical performance was optimized as a function of pre-annealing temperature and AB:PVDF ratio. Temperature programmed desorption (TPD) and Fourier transform infrared (FTIR) spectroscopy indicated both water removal and binder decomposition during heat treatment. However, melting binder rich electrodes appeared to redistribute the conductive additive and create a uniform coating that lead to improved durability. An optimized reversible high capacity of ~1050 mAh g^{-1} was obtained for an electrode fabricated from 70:10:20 active material:AB:PVDF with a 250 °C pre-heat treatment.

1. Introduction

As industry and consumers shift towards implementation of alternative energy sources for both homes and in transportation, there is a greater need for the safe storage of electrical energy. Lithium-ion batteries (LIBs) have shown a strong potential for high performance applications such as in plug-in hybrid electric vehicles (PHEVs) and hybrid electric vehicles (HEVs). Despite their commercial popularity, graphite anodes demonstrate relatively low electrochemical capacities (~372 mAh g^{-1}) [1,2]. In order to be PHEV and HEV compatible, novel electrode materials are needed to improve both energy density and power.

Recent work has focused on nanostructures for improving capacity and rate capability in LIB electrodes [3]. Alcantara et al. fabricated nanocrystalline CoSn by one pot synthesis method and tested the material as an anode [4]. When the particle size was reduced from micron-CoSn, the initial capacities were improved by 500%, close to the theoretical capacity of 664 mAh g^{-1}. Similar results were obtained using Fe_2O_3 as well as $CoSb_3$ [5–7]. Superior rate capabilities for cathodes were achieved by Shaju and Bruce by using a disordered form of nano-Li[$Ni_{0.5}Mn_{1.5}$]O_4 [8]. Our most recent work has employed thin film anodes comprised of nanoparticle MoO_3 [9]. Using electrophoresis deposition on a stainless steel substrate, a stable capacity of 630 mAh g^{-1} was obtained for 150 cycles between 0.005 and 3.5 V. In contrast micron-sized particles of MoO_3 showed significant capacity fade after only several cycles (Fig. 1). These thin films employed neither conductive additive nor binder as in traditional electrodes. Despite stable cycling at a rate of C/2, the reversible capacity was only 60% of the theoretical maximum of MoO_3, 1117 mAh g^{-1}. Also, while thin films may have application in small electronic devices, vehicular applications will likely be comprised of conventional electrodes. Here we report on the optimization of thick (35 μm) electrodes made with MoO_3 as the active material and employing polyvinyl fluorine (PVDF) and acetylene black (AB). The electrodes are tested in a coin cell configuration, that is more relevant to commercial applications. It is found that both the ratio of AB:PVDF and electrode pre-heat treatment are critical to obtaining high reversible capacities and stable cycling. Optimized performance is demonstrated for electrodes that are binder rich (AB:PVDF ratio of 1:2) and heated to 250 °C. The increase in reversible capacity compared to the thin film electrode is attributed to an improved conductive path due to the presence of the AB and melted PVDF polymer chains.

2. Materials and methods

MoO_3 powder was produced by a novel hot-wire chemical vapor deposition (HWCVD) process adapted from Mahan [10] using a single molybdenum 0.5 mm diameter wire from Alfa Aesar. The wire was oxidized in an Ar environment with an O_2 partial pres-

* Corresponding author. Tel.: +1 303 384 6607; fax: +1 303 384 6431.
E-mail address: anne.dillon@nrel.gov (A.C. Dillon).

0378-7753/$ – see front matter © 2009 Elsevier B.V. All rights reserved.
doi:10.1016/j.jpowsour.2009.08.013

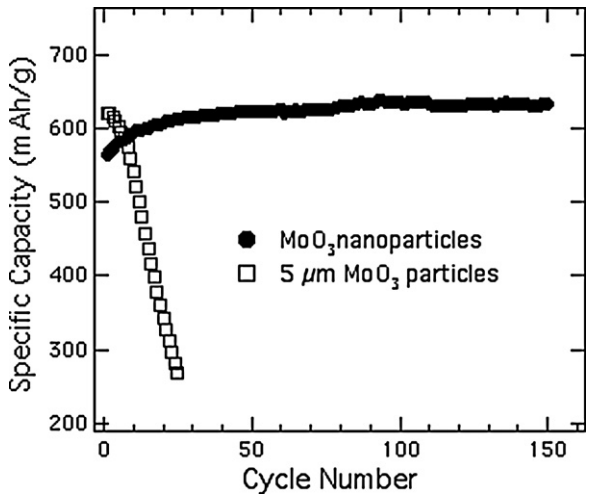

Fig. 1. Specific capacity of nanoparticles with diameters ranging from 5 to 20 nm and the μm-sized particles [9].

sure of ~7% and a total pressure of 75 Torr. Nanoparticles were deposited along a quartz tube reactor heated by a 300 °C clamshell furnace. X-ray diffraction (XRD) to determine the crystal structure of the nano-powders was completed on a Scintag PTS 4-cycle Goniometer operated at 45 kV and 36 mA with an LN_2-cooled Ge X-ray detector. For XRD analysis scans were performed from 10 to 120 at a rate of 0.1° min^{-1} in 0.05° steps. Samples were mounted on stainless steel substrates by an electrophoresis deposition process [11]. A solution of 20 mg powder and 50 mL methanol was sonicated for 5 min to achieve uniform particle suspension. Two stainless steel electrodes were placed 10 cm apart and a voltage of 300 V was applied for 1 min. Particle deposition occurs on the negative electrode. Additional annealing for 2.5 h at 300 °C was performed to fully oxidize the sub-stoichiometric powder. The TEM method for preparation and characterization is also previously described by Mahan et al. [10]. Surface area of the powder was determined using an Autosorb-1 cooled to 75.7 K by LN_2. The Brunauer–Emmett–Teller (BET) method was used to calculate the surface area.

The electrodes were fabricated from a slurry of active material (molybdenum trioxide, MoO_3), a conductive additive, acetylene black, and binder, polyvinyl fluorine from Alfa Aesar. The PVDF was first mixed with water-free N-methyl-2-pyrrolidone (NMP) solvent using a mortar and pestle. The MoO_3 and carbon black was then slowly stirred into the binder and mixed carefully by hand for 15 min. An ~50 μm thick layer of slurry was spread onto 0.019 mm thick copper foil. The copper sheet was allowed to air dry overnight in a single wall gravity convection laboratory oven at 120 °C. To ensure proper electrical contact and increased conductivity, after drying the sheet was calendared with a Durston rolling mill to 75% of the total thickness (35 μm). Electrodes were sized using a 9/16″ diameter punch. Each electrode was heat treated overnight in argon at temperatures ranging between 150 and 300 °C. Lithium metal of equal size was used as the counter electrode. Polymer separators were soaked for at least a week in a 1 M $LiPF_6$ electrolyte solution. Complete cells were assembled in a glove box and then sealed using a Hohsen press. Coin cells were cycled using an Arbin BT2000 from 3.0 to 0.005 V. We used galvanic cycling of constant current on both charge and discharge. The charge and discharge cycle was set at a rate of C/10 for all tests. AC impedane spectroscopy was performed using a Solatron 1280C for a frequency range of 20,000 Hz to 100 mHz.

A Nicolet 510 FTIR Spectrometer was used to collect Fourier transform infrared (FTIR) spectroscopy data. Due to the opacity of the electrode, the reflectivity of the samples was measured using a single beam method. Excess water and CO_2 was purged with nitrogen for at least 20 min prior to background collection in order to minimize signal contamination. The spectrometer was run at an average of 128 scans between 4000 and 400 cm^{-1} at a resolution of 4 cm^{-1}.

The effects of annealing were examined using temperature programmed desorption (TPD). Unheated electrodes were weighed and placed into a clean custom made tube. The quartz tube was attached to the TPD chamber, and a high vacuum was drawn (~10^{-8} Torr), removing any weakly bound species. After excess water and contaminants were pumped from the vial, the sample was heated from room temperature to 350 °C at a rate of ~50° min^{-1}. An SRS RGA-100 mass spectrometer detected the residual gas concentration desorbed from the sample as a function of temperature. The range of detection was 0–100 a.m.u.

3. Results and discussion

The material produced and collected from HWCVD is a fine, black powder, indicating that the particles are sub-stoichiometric. Thus the particles were baked in air at 250 °C to convert the particles to MoO_3. TEM for the MoO_x nanospheres before (Fig. 1a) and after (Fig. 1b) baking indicates that the average particle diameter increases from ~10 up to ~40 nm after annealing. Despite initial signs of particle agglomeration, individual spheres remain identifiable after oxidation. The ideal powder baking temperature and duration were found to be 300 °C for 2.5 h in air. Baking at higher temperatures and/or longer times results in the observance of large micron-sized rods due to increased surface mobility of the atoms. Consistent with the TEM, BET analyses confirm a reduction in surface area of the nanospheres (with the optimal oxidation time) from 49.31 to 28.77 $m^2 g^{-1}$. The change corresponds to an expected 41.65% loss in surface area.

After baking, the powder visually transforms from black to a whitish-blue, which is an indication of oxidation. XRD patterns, in Fig. 2, were used to identify the composition and crystalline structure of the sample. The raw, unbaked powder collected from the HWCVD is indexed as a combination of MoO_2 and Mo metal. Peaks at 44.5° and 65° represent the stainless steel substrate. After baking, the XRD peaks correspond to pristine orthorhombic α-MoO_3 with no significant traces of MoO_2 or Mo metal [12]. The sharp peaks indicate a highly uniform and crystalline structure.

In the electrodes the AB:PVDF ratio was optimized using 70 wt.% MoO_3 to allow for adequate volume expansion during lithiation. Similar to Fe and Si, MoO_3 has a large theoretical volume expansion as lithiation goes to completion which is perhaps tolerated only by nanoparticles [9]. The cells were cycled at room temperature at a charge–discharge rate of C/10 from 3 to 0.005 V. Electrochemical stability and capacity (Fig. 3) were tested using four cell compositions of AB:PVDF (1:2, 1:1.25, 1:1, 2:1). Binder rich electrodes of a 1:2 ratio showed the greatest electrochemical stability near the theoretical capacity, which is in good agreement with previous investigations [15,16]. It appears that large surface area materials such as nanospheres require additional binder in order to maintain physical contact between the active material and the conductive additive. Cell compositions with lower binder content of 1:1 and 2:1 show rapid failure after only eight cycles presumably due to a reduction in conductive pathways for electrons and ions through the electrode.

Electrodes of 70:10:20 composition underwent a minimum of 8 h glove box heat treatment at various temperatures prior to cell construction. As seen in the voltage profiles (Fig. 4a), both no heat treatment and heat treatment at 150 °C result in large first cycle irreversible capacities of nearly 60% likely due to Li^+ reaction with

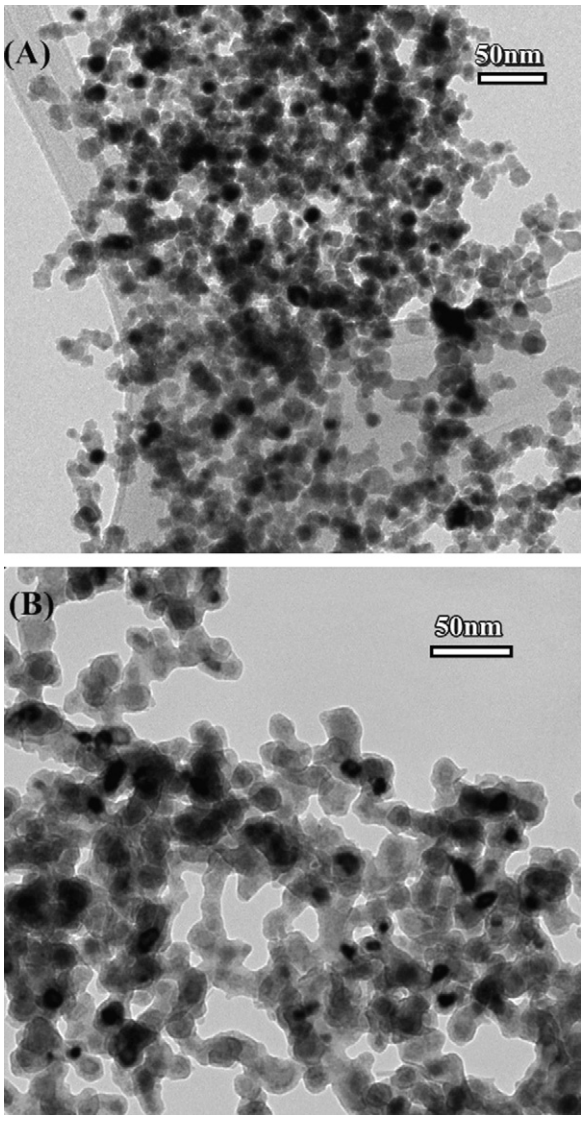

Fig. 2. TEM of MoO_3 nanoparticles (a) before and (b) after baking in air at 250 °C fabricated by HWCVD.

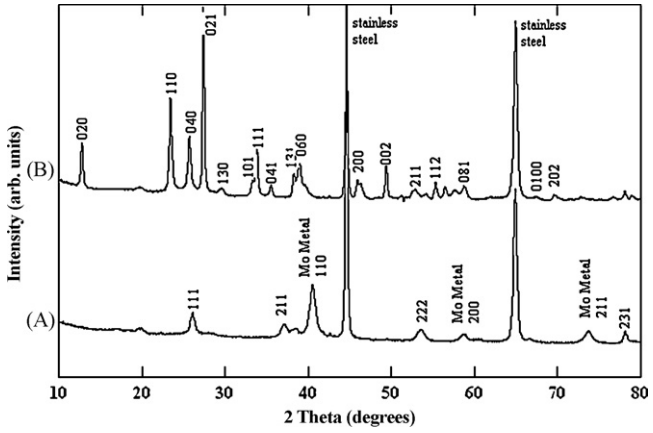

Fig. 3. XRD of nanoparticle powder (a) before and (b) after baking in air at 250 °C. Prior to baking, the powder is a mixture of MoO_2 and Mo metal. After baking, all of the powder is converted to MoO_3.

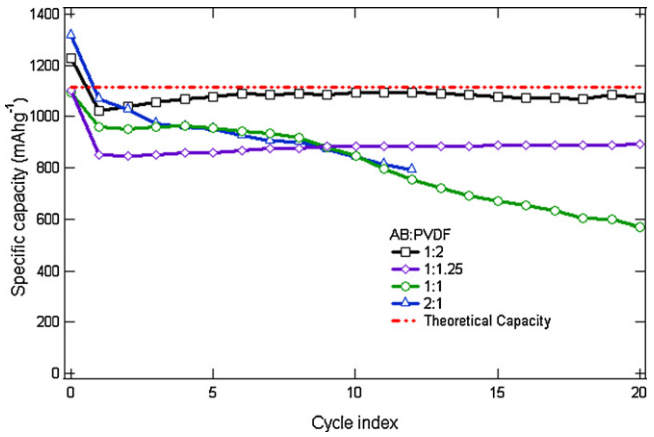

Fig. 4. Effect of AB:PVDF ratio on cycle stability and capacity for 70 wt.% MoO_3.

water. Likewise, both cases show poor cycling stability (Fig. 4b) and rapid degradation. When the pre-annealing temperature was increased beyond 150 °C, the irreversible capacity is significantly reduced. For a heat treatment temperature of 250 °C a stable capacity of ~1050 mAh g^{-1} is observed for 30 cycles. This high reversible capacity corresponds to 80% of the initial capacity of 1400 mAh g^{-1}. The initial capacity of 1400 mAh g^{-1} exceeds the theoretical maximum capacity expected for 6 Li^+/MoO_3 presumably due to initial surface side reactions. Similar results are observed for the pre-heating temperature of 300 °C, but the stable capacity is reduced to ~875 mAh g^{-1}. Fig. 5 shows how the heat treatment affected the AC impedance of the various electrodes. A decrease in the radius of the first semicircle represents a relative decrease in electronic resistance. Apparently, heating electrodes above the binder's melting temperature of 170 °C redistributes and unfurls long chains to allow for improved electrical contact between active material and conductive additive.

The high reversible capacity of ~1050 mAh g^{-1} corresponds to the insertion of ~5.7 Li^+/MoO_3 which approaches the theoretical maximum (6 Li^+/MoO_3). It has been previously suggested that during the first lithium insertion, MoO_3 undergoes an irreversible structural change from the α-phase to an amorphous phase followed by a conversion reaction to form Li_2O and Mo metal ($MoO_3 + 6Li^+ + 6e^- \rightarrow 3Li_2O + Mo$) [13]. However, the amorphization of the material does not alter the overall electrochemical performance of the electrode. Presumably as Li_2O forms and decomposes, the conversion reaction yields nanodispersed particles of Mo metal [14]. Poizot has purposed that small particles, with an increased total number of surface atoms, in turn increase the electrochemical reactivity and make the conversion process reversible [3]. We also suggest that starting with nanoparticles initially better allows for the formation of small metal clusters during the conversion process. This is consistent with the data presented in Fig. 1, where the nanoparticles out perform the larger commercial metal oxide particles in reversibility.

Additional evidence of water removal for both the electrodes with no heat treatment and heat treatment at 150 °C is exhibited in the FTIR spectra in Fig. 6. The pristine MoO_3 powder after exposure to air is shown to have neither adsorbed molecular water that would be indicated by the H_2O scissors mode at 1640 cm^{-1} nor hydrogen bonded hydroxyl groups that would be indicated by a broad O–H stretching vibration (3200–3500 cm^{-1}). When the active material is mixed with AB:PVDF and deposited onto a copper substrate, both the scissors mode of molecular water and the broad peak associated with the O–H stretching vibration are observed indicating that the water source is actually the AB or PVDF. Peaks between 841 and 1403 cm^{-1} are characteristic of the β-phase PVDF

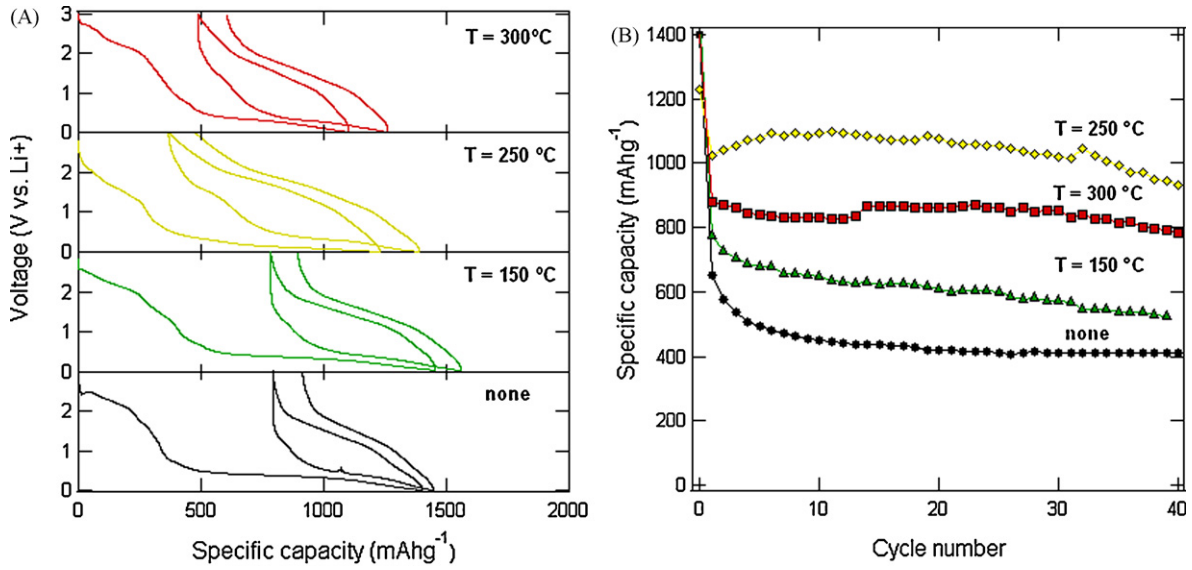

Fig. 5. (a) Cycling profile and (b) performance for cells compositions of 70:10:20 as a function of heat treatment temperature.

[17,18]. After electrode heat treatment to 250 °C, the FTIR shows almost no sign of the scissors mode at 1640 cm^{-1} indicating that molecular water has been removed. The smaller broad feature between 3200 and 3500 cm^{-1} is consistent with stable surface hydroxyl species, possibly now present on the MoO_3 nanoparticle surfaces.

As noted previously, the irreversible Li-insertion that exceeds the theoretical capacity for MoO_3 is most likely due to reactions with surface species. The irreversible insertion is largest for the electrodes not subjected to heat treatment and for the electrode that was only annealed to 150 °C (Fig. 4a). Fig. 6a depicts the TPD spectra of gaseous species desorbing from the electrode while heating in vacuum. Water is observed to desorb from the sample above 70 °C with peak desorption occurring at two temperatures, 100 and 200 °C. The lower desorption peak most likely corresponds to physisorbed H_2O bound to the high surface area MoO_3 and AB. Given the high temperature of the second peak (200 °C), it is likely that stable surface hydroxyl species exist on the MoO_3 nanoparticles. These hydroxyl species then decompose to form water at high temperature. A mechanism for the surface hydroxyl decomposition is shown below:

$$Mo{-}OH + Mo{-}OH \rightarrow Mo{-}O{-}Mo + H_2O$$

The absence of hydrogen evolution with the water desorption supports this surface decomposition mechanism. Water evolution at higher temperature then causes oxidation of the carbon present in the binder and acetylene black, and CO_2 is observed to desorb in the TPD spectrum (Fig. 7a) with the desorption also peaked at 200 °C. The presence of both stable molecular water and surface OH groups inhibit the removal of lithium after initial intercalation, producing the large irreversibility seen in Fig. 4a at lower heat treatment temperatures. For the higher heat treatment temperature of 300 °C, the irreversible capacity is minimized but the total reversible capacity of the material also decreases to ~850 mAh g^{-1} (Fig. 4b). PVDF is a polymer binder consisting of a chain of carbons, alternating with hydrogen and fluorine terminations. As a commercial powder, PVDF melts around 170 °C and decomposes at 375 °C. Independent of MoO_3, AB:PVDF electrodes show initial signs of decomposition, indicated by the desorption of HF, at 350 °C. However, when the metal oxide is added to the composition, binder decomposition begins at a significantly reduced temperature slightly above 250 °C. Previous studies have shown that the addition of metal oxides and

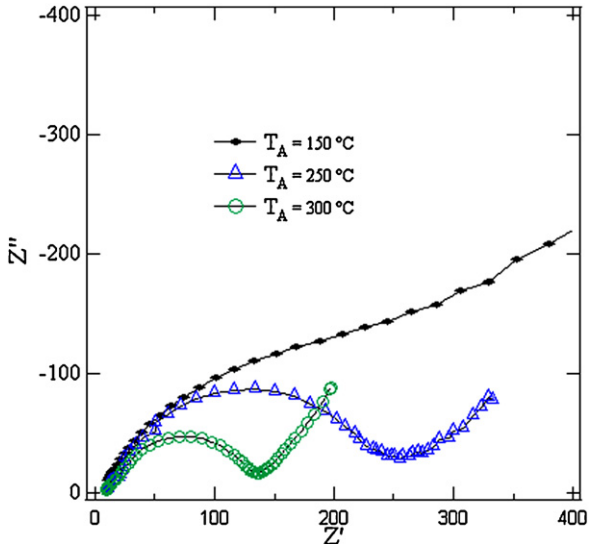

Fig. 6. AC impedance as a function of heat treatment for a 70:10:20 cell composition using MoO_3.

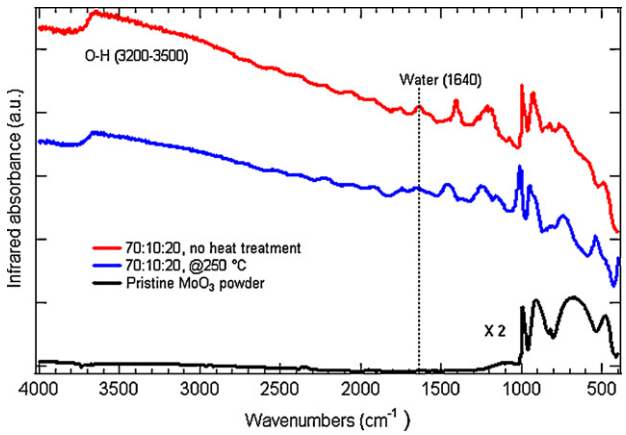

Fig. 7. FTIR of 70:10:20 electrodes on Cu substrate. Molecular water, present prior to heat treatment, is fully removed when annealed up to 250 °C.

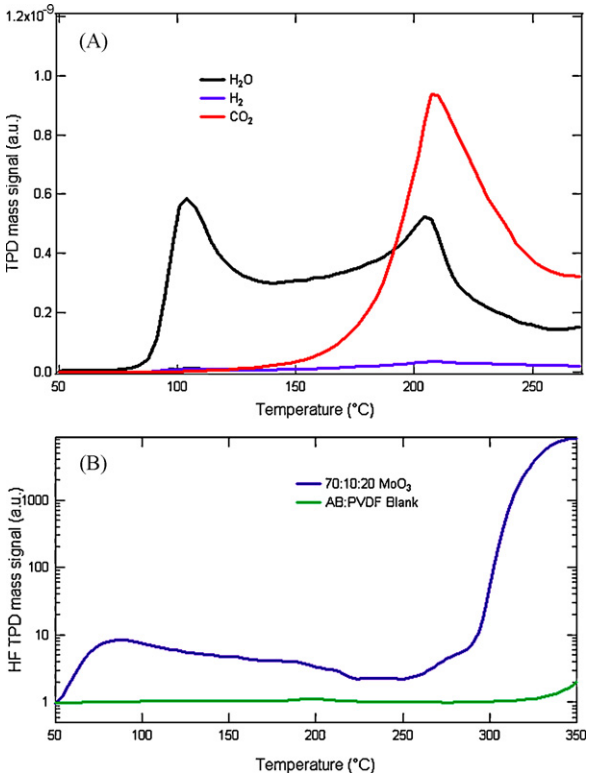

Fig. 8. TPD mass signal as a function of temperature for MoO_3:AB:PVDF composition of 70:10:20 for (a) select desorbed gas species and (b) binder decomposition.

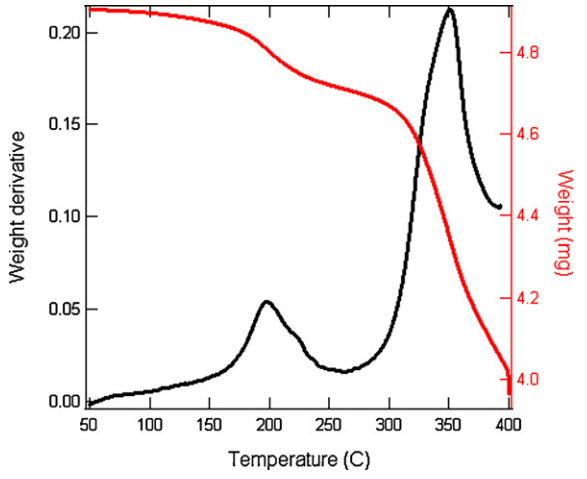

Fig. 9. Thermal gravimetric analysis (TGA) of MoO_3:AB:PVDF, 70:10:20.

nitrides to various polymer compounds accelerates the chain scission within the binder, reducing the decomposition temperature [19–21]. The actual binder degradation temperature is thus dependent upon the active material and its ability to unzip polymer chains [22].

The water removal and early binder decomposition is also supported by TGA (Fig. 8). At 200 °C, the large peak in the weight derivative curve is attributed to both water loss and the conductive additive decomposition due to oxidation. A saddle for the weight change occurs just after 250 °C, followed by a rapid weight loss consistent with the complete binder breakdown. Full decomposition is observed at 350 °C. As identified by TPD in Fig. 7b and supported by the cycling data in Fig. 4, the ideal heat treatment temperature occurs just prior to binder decomposition. For the MoO_3 electrodes, the optimal temperature is 250 °C. Li et al. determined that the ideal heat treatment for Si:PVDF electrodes occurred at 300 °C [23]. We believe that each active material will require a unique optimal annealing temperature that can be easily determined through thermal analysis (Fig. 9).

4. Conclusion

In summary, by using thick, more conventional electrodes of MoO_3 along with AB and PVDF a near-theoretical reversible capacity of ~1050 mAh g^{-1} is obtained. Employing deep charge/discharge, the electrodes maintain a stable capacity for nearly 40 cycles. The optimized electrode composition is 70:10:20 corresponding to MoO_3:AB:PVDF with a pre-heat treatment of 250 °C. A combination of TPD, TGA and IR analyses indicate that water and surface hydroxyl groups may be effectively removed up to 250 °C while annealing the electrode to 300 °C results in binder decomposition.

Acknowledgements

The authors thank Kim Jones for the TEM images. This work was funded by the U.S. Department of Energy under subcontract number DE-AC36-08GO28308 through DOE Office of Energy Efficiency and Renewable Energy Office of the Vehicle Technologies Program.

References

[1] Z.X. Shu, R.S. McMillan, J.J. Murray, I.J. Davidson, Journal of the Electrochemical Society 142 (1995) L161–L162.
[2] A.H. Whitehead, K. Edstrom, N. Rao, J.R. Owen, Journal of Power Sources 63 (1996) 41–45.
[3] P. Poizot, S. Laruelle, S. Grugeon, L. Dupont, J.M. Tarascon, Nature 407 (2000) 496–499.
[4] R. Alcantara, I. Rodriguez, J.L. Tirado, Chemphyschem 9 (2008) 1171–1177.
[5] J. Xie, X.B. Zhao, G.S. Cao, S.F. Su, Journal of the Electrochemical Society 152 (2005) A601–A606.
[6] J. Xie, X.B. Zhao, G.S. Cao, M.J. Zhao, S.F. Su, Journal of Power Sources 140 (2005) 350–354.
[7] B.T. Hang, I. Watanabe, T. Doi, S. Okada, J.I. Yamaki, Journal of Power Sources 161 (2006) 1281–1287.
[8] K.M. Shaju, P.G. Bruce, Dalton Transactions (2008) 5471–5475.
[9] S.H. Lee, Y.H. Kim, R. Deshpande, P.A. Parilla, E. Whitney, D.T. Gillaspie, K.M. Jones, A.H. Mahan, S.B. Zhang, A.C. Dillon, Advanced Materials 20 (2008) 3627–3632.
[10] A.H. Mahan, P.A. Parilla, K.M. Jones, A.C. Dillon, Chemical Physics Letters 413 (2005) 88–94.
[11] A.C. Dillon, A.H. Mahan, R. Deshpande, R. Parilla, K.M. Jones, S.H. Lee, Thin Solid Films 516 (2008) 794–797.
[12] A.D. Sayede, T. Amriou, M. Pernisek, B. Khelifa, C. Mathieu, Chemical Physics 316 (2005) 72–82.
[13] T. Tsumura, M. Inagaki, Solid State Ionics 104 (1997) 183–189.
[14] M.J. Aragon, B. Leon, C.P. Vicente, J.L. Tirado, Journal of Power Sources 189 (2009) 823–827.
[15] A. Timmons, J.R. Dahn, Journal of the Electrochemical Society 154 (2007) A444–A448.
[16] S.D. Beattie, D. Larcher, M. Morcrette, B. Simon, J.M. Tarascon, Journal of the Electrochemical Society 155 (2008) A158–A163.
[17] A.K. Gupta, R. Bajpai, J.M. Keller, Journal of Polymer Research 15 (2008) 275–283.
[18] C.L. Wang, J.C. Li, W.L. Zhong, P.L. Zhang, Q.H. Wang, IR Vibrational Modes of PVDF Chains, 2003, 469–470.
[19] K.J. Kim, Y. Doi, H. Abe, Polymer Degradation and Stability 93 (2008) 776–785.
[20] P. Malik, M. Castro, C. Carrot, Polymer Degradation and Stability 91 (2006) 634–640.
[21] M. Abdelaziz, Journal of Magnetism and Magnetic Materials 279 (2004) 184–194.
[22] Y.J. Fan, H. Nishida, T. Mori, Y. Shirai, T. Endo, Polymer 45 (2004) 1197–1205.
[23] J. Li, L. Christensen, M.N. Obrovac, K.C. Hewitt, J.R. Dahn, Journal of the Electrochemical Society 155 (2008) A234–A238.